Cryo2S1: Cross-Sensor Representation Learning for Sea Ice Radar Freeboard and Leads in Sentinel-1 SAR

Andreas Stokholm
DTU Space, Department of
Space Research and Space Technology
Technical University of Denmark
Kgs. Lyngby, 2800, Denmark
stokholm@space.dtu.dk

Jack Christopher Landy
Department of Physics and Technology
UiT, The Arctic University of Norway
Tromsø, 9019, Norway
jack.c.landy@uit.no

Tore Wulf
DMI, Danish Meteorological Institute
Copenhagen, 2100, Denmark
twu@dmi.dk

Roberto Saldo
DTU Space, Department of
Space Research and Space Technology
Technical University of Denmark
Kgs. Lyngby, 2800, Denmark
rs@space.dtu.dk

Peter Naylor
Φ-Lab, European Space Research Institute
European Space Agency
Frascati, 00044, Italy
peter.naylor@esa.int

Nicolas Longépé
Φ-Lab, European Space Research Institute
European Space Agency
Frascati, 00044, Italy
nicolas.longepe@esa.int

Sine Munk Hvidegaard
DTU Space, Department of
Space Research and Space Technology
Technical University of Denmark
Kgs. Lyngby, 2800, Denmark
smh@space.dtu.dk

Abstract

Monitoring Arctic sea ice is essential for understanding climate dynamics, improving weather prediction, and ensuring safe maritime navigation. While Sentinel-1 (S1) C-band Synthetic Aperture Radar (SAR) imagery offers high-resolution and wide coverage, it only provides surface-level information. Contrary, CryoSat-2 (CS2) Ku-band SAR altimetry provides sea ice radar freeboard measurements fundamental for estimating sea ice thickness using hydrostatic principles, but suffers from sparse spatiotemporal coverage. Here, we propose a supervised deep learning framework, fusing S1 imagery with CS2 line data to map radar freeboard and leads by learning cross-sensor representations, enabling high-resolution and broad coverage of these sea ice properties. Our model achieves a mean absolute error of 4.1 cm for radar freeboard and 95.7% overall accuracy in sea ice/lead classification. The model shows promising generalisation and strong spatial alignment between mapped sea ice properties and observed SAR image features. This paves the way for large-scale and temporally rich sea ice monitoring using existing satellite records for assimilation of C-band SAR-derived sea ice products into climate and weather models and for operational navigation products.

1 Introduction

The Arctic Ocean is a highly dynamic environment, where sea ice constantly grows, melts, and moves. As a key component of Earth's climate system, sea ice reflects sunlight, insulates the ocean, and influences heat and moisture exchange [1]. Hence, sea ice is crucial to monitor for assessing the state of the climate, for weather prediction, and to safely and efficiently navigate along the Northern trade routes [2]. Sea ice thickness and sea ice openings, known as *leads*, are essential variables. Thickness enables the assessment of the sea ice volume and when the Arctic will become ice-free, while leads influence heat and moisture exchange between the ocean and the atmosphere.

The extent and conditions of sea ice are widely monitored with the Sentinel-1 (S1) Synthetic Aperture Radar (SAR) constellation due to its broad coverage, high-latitude acquisitions (up to 87.5°N), short revisit times, and high spatial resolution and versatile year-round observations [3]. S1 imagery and deep learning have been used extensively to map sea ice surface properties [4, 5, 6, 7, 8, 9, 10, 11]. However, estimating thickness from S1 is challenging as the C-band radar wave is scattered at the ice surface. Furthermore, current AI sea ice SAR datasets [12, 13] rely on manually derived sea ice charts with sea ice concentration without small-scale features, such as leads [8].

Current state-of-the-art sea ice thickness retrieval methods rely on altimeters like CryoSat-2 (CS2) to measure the elevation between the sea ice and the ocean surfaces, known as the sea ice freeboard [14]. The sea ice freeboard converts to thickness using hydrostatic equilibrium principles [15]. For a Ku-band SAR altimeter like CS2, it is assumed that the radar response penetrates the snow and returns from the sea ice surface. As the true penetration is unknown, and the radar wave propagation is delayed when the signal passes through snow, the measured quantity is known as the radar freeboard [14]. With this approach, the sea ice thickness can be estimated with an accuracy of 20-40% using the radar freeboard by calculating the sea ice's buoyancy based on hydrostatic equilibrium, where snow and ice density estimates, and auxiliary snow depth information are accounted for. To get the ocean height measurement, leads are often measured and thus classified. However, CS2 only measures 1600m across-track and can thus only monitor sea ice thickness in the Arctic monthly, insufficient for e.g. maritime navigation, and leaves data record gaps. S1 SAR, on the other hand, cover up to 400km mode across-track with repeating coverage every week.

To circumvent the limitations of S1 and CS2, we train supervised deep learning models to learn cross-sensor representations of sea ice to map CS2-measured sea ice radar freeboard and leads in S1 images. This fuses the two sensor modalities to gain the advantage of both with the large coverage of S1, while expanding the capabilities to map sea ice radar freeboard and leads enabled by CS2.

2 Data

This study utilises the Cryo2S1 dataset with crossover satellite S1 SAR images and CS2 altimetry line data collected in the winter season of January–April and October–December in 2020 and 2021. The Copernicus S1 A and B (available in this time period) SAR satellites, launched in 2014 and 2016, respectively, operated by the European Space Agency (ESA), operate at a 5.4 GHz frequency C-band (5.5 cm wavelength) [3]. Here, the level-1 Ground Range Detected (GRD) product is used in high-resolution 20x22m, 10m pixel spacing Interferometric Wide Swath (IW) and medium-resolution 87x93m, 40m pixel spacing Extra Wide (EW) modes, processed with ESA IPF v3.2–4 (depending on acquisition time), incorporating noise correction [16, 17]. The two-channel dual polarised HH and HV, and measurement incidence angles are included. The S1 IW images are up to $\sim$25,000$\times$25,000 and $\sim$10,000$\times$10,000 pixels for EW.

ESA's CS2 was launched in 2010 with the 13.6 GHz Ku-Band Interferometric Radar ALtimeter (SIRAL) [18]. Three sensor modes are available. Here, the operation mode is limited to SAR. The baseline E is used and processed according to Landy et al. [19, 20] applied in regions with a minimum of 15% sea ice concentration. The data includes sea ice radar freeboard and lead classification.

The curated dataset consists of scenes with a temporal overlap of $\pm$1 hour between S1 and CS2, covering the entire Arctic Ocean, as illustrated in Fig. 1**a)**, with most scenes located North of Greenland. The final dataset comprises 4,516 crossover scenes, split into 3,866 for training, 219 for validation, and 431 for testing across the time period. The validation and test sets are selected to represent the entire Arctic with a similar geographical footprint to the training dataset. An example of a crossover scene is illustrated in Fig. 1**b)**.

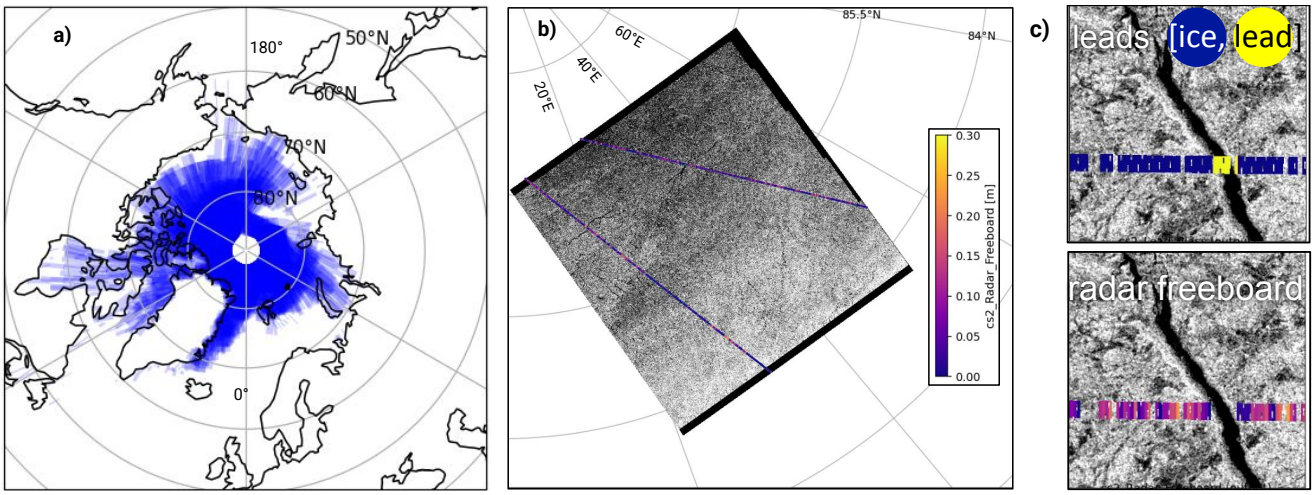

Figure 1: **Data overview**. **a)**: spatial distribution of the SAR data. Blue colour intensity illustrates spatially overlapping scenes. **b)**: S1 SAR HH image acquired on October 2nd 2021, close to the geographical North Pole, overlaid with two sea ice radar freeboard values CS2 tracks. **c)**: Crop of an S1 HH image overlaid with CS2 sea ice radar freeboard and lead classifications over a sea ice lead.

We further preprocess the data using the same setup as in [8] with S1 data prepared by subtracting the mean and scaling with the standard deviation (STD) from the individual channels calculated across the training data. The same mean and STD are utilised for both the S1 SAR HH and HV channels to retain the discrepancy in backscatter intensities, inspired by Wulf et al. [10]. S1 pixels without information are set to 0, and locations are retained in a mask for each S1 scene.

The CS2 reference is generated in the S1 image dimensions, and CS2 observations are projected onto the S1 image. As the exact CS2 measurement location is unknown within the 1,600×333m footprint, all the corresponding S1 pixels within the CS2 footprint are given the same CS2 variable value. This is illustrated in Fig. 1**c)**. Note that radar freeboard values are unavailable in detected leads. Reference pixels without CS2 values are set to -1. The distribution of lead classifications is heavily skewed towards sea ice pixels, with less than 10% of pixels classified as leads.

Batches are generated by randomly sampling 32 1024×1024 pixel patches. Each scene has a probability of being sampled corresponding to its percentage of CS2 freeboard values with respect to the total number of CS2 freeboard values in the total training dataset. One patch is sampled at each weighted scene draw. During random patch cropping, the centre crop and ±100 pixels from the nearest reference value have an equal probability of being sampled, while other pixels have a zero percentage sampling probability. This is inspired by Stokholm et al. [6].

Each batch is augmented with a random set of augmentations, one for each patch, and identical across S1 and the CS2 reference. We utilise the dihedral group: 0, 90, 180 or 270-degree rotations, as well as horizontal, vertical and two diagonal flips, i.e. 8 in total, random-sized crop within the patch using a scaling within 25-85%, and coarse dropout with 1-8 holes sized between 8-64×8-64 pixels.

3 Methods

Here, the U-Net [21] CNN architecture is used with 6 encoder-decoder blocks (24 and 48 filters in the first two and 64 filters in the rest) and trained with 1000 batches for 100 epochs. The Adam optimiser is utilised with a learning rate of 0.0001 and default PyTorch hyperparameters, $\beta_1 = 0.9, \beta_2 = 0.999$. The loss used for the radar freeboard optimisation is the Mean Squared Error (MSE) and Binary Cross Entropy (BCE) for lead classification. The loss of each patch in the batch is scaled by the ratio of valid pixels to masked pixels, giving larger weight to patches with more valid pixels. After each epoch, the model is validated, and the model parameters are stored. The epoch model parameters with the lowest validation loss are selected for testing and inference. The model is evaluated on the test set using the Mean Absolute Error (MAE) for the radar freeboard and binary accuracy for lead classification. Inference is applied on 3,072×3,072 patches with an overlap of 50% and stitching of the crop series using the 1,536×1,536 centre to mitigate the influence of padding, inspired by Huang et al. [22].

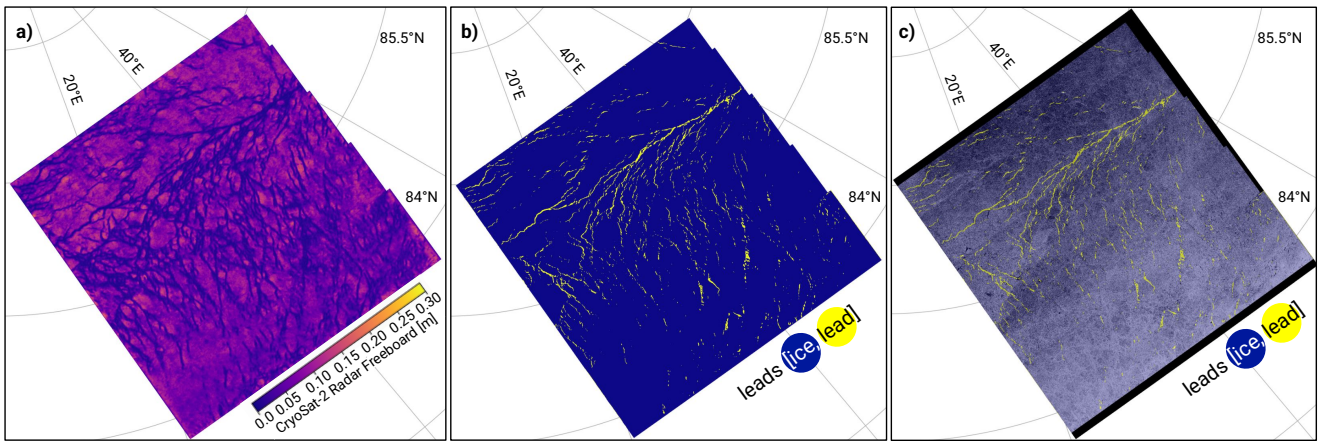

Figure 2: **Inference results** applied to the SAR scene in Fig. 1**b)** acquired on October 2nd 2021. **a)**: sea ice radar freeboard in meters. **b)**: sea ice lead classification. **c)**: sea ice lead classification with visualisation alpha for sea ice=0.2 and lead=0.5, highlighting the leads.

4 Results & Discussion & Future Work

The trained model applied to the test set achieves a sea ice radar freeboard MAE of 4.1 cm, showing the model's capacity to produce realistic values that align with the reference. Illustrated in Fig. 2**a)** is the model sea ice radar freeboard inference on the scene in Fig. 1**b)** (test scene). The radar freeboard inference appears to clearly demarcate floes with areas of low freeboard surrounding them. In a diagonal line North of 85.5°, a shear zone is evident, aligning well with the SAR image in Fig. 1**b)**. The inference appears to exhibit additional zones of low freeboard compared to dark areas in the SAR. This can be explained by areas of previous leads that have frozen and, therefore, have a lower thickness and thus a lower freeboard compared to the surrounding sea ice. Several areas of higher freeboard are also present that could indicate rafts, ridges or hummocks, and typically appear as bright features compared to surrounding backscatter intensities.

The sea ice radar freeboard SAR inference appears viable for computing sea ice thickness using hydrostatic equilibrium with well-known ocean and snow density values, and numerical model values for snow depth, e.g. Liston et al. [23]. Furthermore, sea ice density values for sea ice types are known. The stage of development, a proxy for sea ice type, is attainable in SAR imagery with deep learning as shown in Stokholm et al. [8], and could improve the sea ice thickness estimation. The inferred leads, radar freeboard and computed sea ice thickness can be further evaluated by comparing with airborne campaign data (e.g. CryoVEx or Operation IceBridge), or in-situ data, such as buoys or ship-based observations [24] or other satellite data like ICESat-2 [25] or Sentinel-3 [26].

The model lead classification achieves 95.7% overall accuracy, with 98.9% accuracy for ice and lead accuracy of 37.7%. Initially, the lead accuracy appears discouraging, but several factors the result. As the dataset's lead class distribution is heavily skewed towards sea ice, the model is rewarded more to get sea ice correct, emphasising the lead class less. Using class weights in the loss computation could mitigate this. Another reason is that all pixels within a CS2 measurement footprint are given the same class. Sometimes, a pixel classified as a lead in the dataset can be on sea ice when leads are narrow or when oriented diagonally compared with the CS2 track, as illustrated in Fig. 1**c)**. This can also occur for the radar freeboard reference. Resolving this could be by using a smaller CS2 footprint, e.g. reducing the across-track width from 1,600m to 1,200m. Furthermore, the altimeter is precise and can detect small leads that are difficult to distinguish in the SAR images, as this requires contrast between several pixels in the SAR images. Another challenge is the sea ice drift between the two satellite acquisitions, which can be up to 1 hour. In a worst-case scenario, sea ice could have moved 2km, translating into 50 pixels in S1 EW mode. However, on an hourly basis, an average of 200m is more likely, translating into 5 pixels, which is well within the uncertainty related to the CS2 footprint itself. Despite the low lead accuracy, inspecting the inferred lead classification, illustrated in Fig. 2**b)**, is encouraging, with classified leads aligning with areas of low freeboard in Fig. 2**a)**, particularly in the shear zone above 85.5°. The lead classification overlaid the S1 image illustrated in Fig. 2**c)** highlights a strong overlap between dark cracks in the ice, representing leads. While dark areas not classified as leads remain, the immediate result is promising.

The lead classification appears impactful, either to be used directly in numerical climate and weather models or as an initial step, with further manual refining, to generate a dataset for sea ice lead detection in an S1 SAR dataset, which is otherwise a labour-intensive process. Here, the S1 lead dataset would not be limited by crossovers with CS2, enabling a dataset orders of magnitude larger.

Increasing the number of leads in the Cryo2S1 dataset could further improve the accuracy performance. The current dataset has two winter seasons, and additional crossover data is obtainable, as S1 and CS2 have been in orbit simultaneously for more than 10 years, enabling the extension of the dataset by up to 8 times. Additionally, other satellite SAR altimeters, such as Sentinel-3, could be included. The current Cryo2S1 dataset is focused on winter sea ice, as applying the CS2 processing chain to summer sea ice, where features, such as melt ponds, complicate the process. When summer CS2 data are reliable, the dataset could be further expanded to include full years, doubling the size. Further developments in model architecture to incorporate attention-mechanisms or other network building blocks, could also help facilitate improved model performance.

5 Conclusion

This study demonstrates the potential of combining CryoSat-2 SAR altimetry line data and Sentinel-1 SAR imagery using supervised deep learning to resolve the limitations of each individual sensor for sea ice mapping. By enabling the model to learn cross-sensor representations, it is possible to successfully infer realistic sea ice radar freeboard with a mean absolute error of 4.1 cm, and the lead classification aligns well with physical features such as shear zones and low freeboard areas, indicating promising avenues for operational applications. Although lead detection accuracy remains low due to the class imbalance and spatial resolution differences. The approach enables scalable mapping of sea ice thickness and leads to produce decade-long time series of sea ice thickness and lead records in the Arctic in 10-40m resolution with sub-weekly instead of monthly time resolution. Such time series are imperative for assimilation into climate and weather, and for Arctic ship navigation to improve voyage efficiency and safety in the remote Arctic Ocean, in support of the Northern trade routes. Future work will focus on expanding the dataset across seasons and incorporating additional altimeter missions to further improve model robustness and coverage.

References

[1] Walter N. Meier, Alek Petty, Stefan Hendricks, Angela Bliss, Lars Kaleschke, Dmitry Divine, Sinead Farrel, Sebastian Gerland, Donald Perovich, Robert Ricker, Xian Tian-Kunze, and Melinda Webster. Noaa Arctic Report Card 2024 : Sea Ice. *National Oceanic and Atmospheric Administration*, 2024. https://doi.org/10.25923/aksk-7p66.

[2] Eddy Bekkers, Joseph F. Francois, and Hugo RojasRomagosa. Melting ice Caps and the Economic Impact of Opening the Northern Sea Route. *The Economic Journal*, 128(610): 1095–1127, aug 18 2017. https://doi.org/10.1111/ecoj.12460.

[3] Ramon Torres, Paul Snoeij, Dirk Geudtner, David Bibby, Malcolm Davidson, Evert Attema, Pierre Potin, BjÖrn Rommen, Nicolas Floury, Mike Brown, Ignacio Navas Traver, Patrick Deghaye, Berthyl Duesmann, Betlem Rosich, Nuno Miranda, Claudio Bruno, Michelangelo L'Abbate, Renato Croci, Andrea Pietropaolo, Markus Huchler, and Friedhelm Rostan. Gmes Sentinel-1 mission. *Remote Sensing of Environment*, 120:9–24, 5 2012. http://doi.org/10.1016/j.rse.2011.05.028.

[4] Lei Wang, K. Scott, and David Clausi. Sea Ice Concentration Estimation during Freeze-Up from SAR Imagery Using a Convolutional Neural Network. *Remote Sensing*, 9(5):408, apr 26 2017. https://doi.org/10.3390/rs9050408.

[5] David Malmgren-Hansen, Leif Toudal Pedersen, Allan Aasbjerg Nielsen, Matilde Brandt Kreiner, Roberto Saldo, Henning Skriver, John Lavelle, Jorgen Buus-Hinkler, and Klaus Harnvig Krane. A Convolutional Neural Network Architecture for Sentinel-1 and AMSR2 Data Fusion. *IEEE Transactions on Geoscience and Remote Sensing*, 59(3):1890–1902, 3 2021. https://doi.org/10.1109/tgrs.2020.3004539.

[6] Andreas Stokholm, Tore Wulf, Andrzej Kucik, Roberto Saldo, Jorgen Buus-Hinkler, and Sine Munk Hvidegaard. AI4SeaIce: Toward solving ambiguous SAR textures in convolutional

neural networks for automatic sea ice concentration charting. *IEEE Transactions on Geoscience and Remote Sensing*, 60:1–13, 2022. https://doi.org/10.1109/tgrs.2022.3149323.

[7] Andrzej Kucik and Andreas Stokholm. AI4SeaIce: Selecting loss functions for automated SAR sea ice concentration charting. *Scientific Reports*, 13(1), apr 12 2023. http://doi.org/10.1038/s41598-023-32467-x.

[8] Andreas Stokholm, Jørgen Buus-Hinkler, Tore Wulf, Anton Korosov, Roberto Saldo, Leif Toudal Pedersen, David Arthurs, Ionut Dragan, Iacopo Modica, Juan Pedro, Annekatrien Debien, Xinwei Chen, Muhammed Patel, Fernando Jose Pena Cantu, Javier Noa Turnes, Jinman Park, Linlin Xu, Katharine Andrea Scott, David Anthony Clausi, Yuan Fang, Mingzhe Jiang, Saeid Taleghanidoozdoozan, Neil Curtis Brubacher, Armina Soleymani, Zacharie Gousseau, Michał Smaczny, Patryk Kowalski, Jacek Komorowski, David Rijlaarsdam, Jan Nicolaas van Rijn, Jens Jakobsen, Martin Samuel James Rogers, Nick Hughes, Tom Zagon, Rune Solberg, Nicolas Longépé, and Matilde Brandt Kreiner. The AutoICE challenge. *The Cryosphere*, 18(8): 3471–3494, aug 7 2024. http://doi.org/10.5194/tc-18-3471-2024.

[9] Xinwei Chen, Muhammed Patel, Fernando J. Pena Cantu, Jinman Park, Javier Noa Turnes, Linlin Xu, K. Andrea Scott, and David A. Clausi. Mmseaice: a collection of techniques for improving sea ice mapping with a multi-task model. *The Cryosphere*, 18(4):1621–1632, apr 8 2024. https://doi.org/10.5194/tc-18-1621-2024.

[10] Tore Wulf, Jørgen Buus-Hinkler, Suman Singha, Hoyeon Shi, and Matilde Brandt Kreiner. Pan-Arctic sea ice concentration from SAR and passive microwave. *The Cryosphere*, 18(11): 5277–5300, nov 19 2024. https://doi.org/10.5194/tc-18-5277-2024.

[11] Xinwei Chen, Muhammed Patel, Linlin Xu, Yuhao Chen, K. Andrea Scott, and David A. Clausi. A Weakly Supervised Learning Approach for Sea Ice Stage of Development Classification From AI4Arctic Sea Ice Challenge Dataset. *IEEE Transactions on Geoscience and Remote Sensing*, 63:1–15, 2025. https://doi.org/10.1109/tgrs.2025.3542803.

[12] Roberto Saldo, Matilde Brandt Kreiner, Jørgen Buus-Hinkler, Leif Toudal Pedersen, David Malmgren-Hansen, Allan Aasbjerg Nielsen, and Henning Skriver. AI4Arctic / ASIP Sea Ice Dataset - Version 2. *data.dtu.dk*, 2021. https://doi.org/10.11583/DTU.13011134.v3.

[13] Jørgen Buus-Hinkler, Tore Wulf, Andreas Stokholm, Anton Korosov, Roberto Saldo, Leif Toudal Pedersen, David Arthurs, Rune Solberg, Nicolas Longépé, and Matilde Brandt Kreiner. Ai4arctic sea ice challenge dataset. *data.dtu.dk*, 2022. https://doi.org/10.11583/DTU.c.6244065.v2.

[14] Jack C. Landy, Jens K. Ehn, David G. Babb, Nathalie Thériault, and David G. Barber. Sea ice thickness in the Eastern Canadian Arctic: Hudson Bay Complex &; Baffin Bay. *Remote Sensing of Environment*, 200:281–294, 10 2017. http://doi.org/10.1016/j.rse.2017.08.019.

[15] R. Ricker, S. Hendricks, V. Helm, H. Skourup, and M. Davidson. Sensitivity of CryoSat-2 Arctic sea-ice freeboard and thickness on radar-waveform interpretation. *The Cryosphere*, 8(4): 1607–1622, aug 28 2014. http://doi.org/10.5194/tc-8-1607-2014.

[16] Kersten Schmidt, Marco Schwerdt, Guillaume Hajduch, Pauline Vincent, Andrea Recchia, and Muriel Pinheiro. Radiometric Re-Compensation of Sentinel-1 SAR Data Products for Artificial Biases due to Antenna Pattern Changes. *Remote Sensing*, 15(5):1377, feb 28 2023. https://doi.org/10.3390/rs15051377.

[17] SAR Mission Performance Cluster. Sentinel-1 MPC. https://sar-mpc.eu/processor/ipf/ [Online; accessed 2025-10-13].

[18] T Geminale, F Carriero, J Bouffard, and T Parrinello. Cryosat product handbook baseline E. Technical report, The European Space Agency, 2021.

[19] Jack C. Landy, Alek A. Petty, Michel Tsamados, and Julienne C. Stroeve. Sea Ice Roughness Overlooked as a Key Source of Uncertainty in CryoSat-2 Ice Freeboard Retrievals. *Journal of Geophysical Research: Oceans*, 125(5), 5 2020. https://doi.org/10.1029/2019jc015820.

[20] Jack C. Landy, Claude de Rijke-Thomas, Carmen Nab, Isobel Lawrence, Isolde A. Glissenaar, Robbie D. C. Mallett, Renée M. Fredensborg Hansen, Alek Petty, Michel Tsamados, Amy R. Macfarlane, and Anne Braakmann-Folgmann. Anticipating CRISTAL: An exploration of multi-frequency satellite altimeter snow depth estimates over Arctic sea ice, 2018–2023. Technical report, Copernicus GmbH, sep 25 2024. https://doi.org/10.5194/egusphere-2024-2904.

[21] Olaf Ronneberger, Philipp Fischer, and Thomas Brox. *U-net: Convolutional networks for biomedical image segmentation*, pages 234–241. Springer International Publishing, Cham, 2015. https://doi.org/10.1007/978-3-319-24574-4_28.

[22] Bohao Huang, Leslie M. Collins, Kyle Bradbury, and Jordan M. Malof. Deep convolutional segmentation of remote sensing imagery: A simple and efficient alternative to stitching output labels. In *IGARSS 2018 - 2018 IEEE International Geoscience and Remote Sensing Symposium*. IEEE, 7 2018. https://doi.org/10.1109/igarss.2018.8518701.

[23] Glen E. Liston, Polona Itkin, Julienne Stroeve, Mark Tschudi, J. Scott Stewart, Stine H. Pedersen, Adele K. Reinking, and Kelly Elder. A Lagrangian SnowEvolution System for SeaIce Applications (SnowModelLG): Part I—Model Description. *Journal of Geophysical Research: Oceans*, 125(10), 10 2020. https://doi.org/10.1029/2019jc015913.

[24] Ida Birgitte Lundtorp Olsen, Henriette Skourup, Heidi Sallila, Stefan Hendricks, Renée Mie Fredensborg Hansen, Stefan Kern, Stephan Paul, Marion Bocquet, Sara Fleury, Dmitry Divine, and Eero Rinne. Dual-hemisphere sea ice thickness reference measurements from multiple data sources for evaluation and product inter-comparison of satellite altimetry. Technical report, Copernicus GmbH, oct 24 2024. https://doi.org/10.5194/essd-2024-234.

[25] R. Kwok, S. Kacimi, T. Markus, N. T. Kurtz, M. Studinger, J. G. Sonntag, S. S. Manizade, L. N. Boisvert, and J. P. Harbeck. Icesat2 Surface Height and Sea Ice Freeboard Assessed With ATM Lidar Acquisitions From Operation IceBridge. *Geophysical Research Letters*, 46(20): 11228–11236, oct 28 2019. https://doi.org/10.1029/2019gl084976.

[26] Jérémie Aublanc, Julien Renou, Fanny Piras, Karina Nielsen, Stine K. Rose, Sebastian B. Simonsen, Sara Fleury, Stefan Hendricks, Nicolas Taburet, Giovanni D'Apice, Anouk Chamayou, Pierre Féménias, Filomena Catapano, and Marco Restano. Sentinel-3 Altimetry Thematic Products for Hydrology, Sea Ice and Land Ice. *Scientific Data*, 12(1), apr 29 2025. https://doi.org/10.1038/s41597-025-04956-3.